Effect of technological voids on the swelling behaviour of compacted bentonite/claystone mixture

Zhixiong Zeng, Yu-Jun Cui, Feng Zhang, Nathalie Conil, Jean Talandier

Effect of technological voids on the swelling behaviour of compacted bentonite/claystone mixture

Zhixiong Zeng[1], Yu-Jun Cui[1*], Feng Zhang[1], Nathalie Conil[2], Jean Talandier[3]

1: Ecole des Ponts ParisTech, Laboratoire Navier/CERMES, 6 et 8 avenue Blaise Pascal, 77455 Marne La Vallée cedex 2, France
2: Andra, Centre de Meuse/Haute-Marne, RD 960, 55290 Bure, France
3: Andra, 1/7, rue Jean Monnet, 92298 Châtenay-Malabry cedex, France

***Corresponding author**

Professor Yu-Jun Cui

Ecole des Ponts ParisTech, Laboratoire Navier/CERMES, 6 – 8 av. Blaise Pascal, Cité Descartes, Champs-sur-Marne, 77455 Marne – la – Vallée cedex 2, France
Tel.: +33 164153550
Fax: +33 164153562
E-mail address: yu-jun.cui@enpc.fr

Abstract: The effect of technological voids on the swelling pressure of compacted MX80 bentonite-Callovo-Oxfordian (COx) claystone mixture was investigated by simulating the technological voids with a pre-defined space between the compacted disks of the mixture. Both axial and radial swelling pressures were monitored. After the tests, the microstructure of samples at different positions was investigated using Mercury Intrusion Porosimetry (MIP), together with the determination of dry density and water content. Results showed that two main processes, filling and homogenization, occurred during soil hydration. In the filling process, the initial technological voids were gradually filled and the axial swelling pressure tended to increase. In the homogenization process, the samples had a sealing zone and a swelling zone. The sealing zone was characterized by a lower dry density than the expected final dry density while the swelling zone was characterized by a larger one. From the MIP results, the sealing zone showed larger inaccessible-pore, medium-pore and large-pore void ratios and a lower small-pore void ratio than the swelling zone. Over time, the medium and large pores in the sealing zone were compressed, while the small pores in the swelling zone decreased. The stabilized axial swelling pressure followed a unique relationship with the expected final dry density. Moreover, the swelling pressure anisotropy was found to decrease as the technological voids increased.

Keywords: bentonite-claystone mixture; technological voids; swelling pressure; swelling anisotropy; microstructure

1 Introduction

In the context of deep geological disposal for radioactive waste, pre-compacted blocks of bentonite-based materials are often considered as possible sealing and backfilling materials thanks to their high swelling capacity, low permeability and favourable radionuclide migration retardation properties (Pusch, 1982; Dixon et al., 1985; Komine and Ogata, 1994; 1999; Cui, 2017). When the compacted blocks are placed in the disposal galleries, radially technological voids between the blocks, the canisters, and the host rock, and axially technological voids between the blocks themselves are unavoidable (Wang et al., 2013a). Upon contact with pore water from the host rock, compacted blocks will swell and fill up the technological voids, leading to a decrease of dry density. After that, swelling pressure will develop both radially and axially (Pusch, 1982; Saba et al., 2014a). Previous studies (Villar et al., 2005; Gen et al., 2011; Wang et al., 2013a) showed that after the saturation process, the initial heterogeneity could remain to some extent, significantly affecting the hydromechanical behaviour of the sealing and backfilling materials. From the practical point of view, it is essential to well understand the swelling behaviour of compacted blocks upon hydration, in particular in case of presence of technological voids.

The effect of technological voids on the swelling behaviour of compacted sealing and backfilling materials has been widely investigated in both the laboratory and the field, in terms of swelling pressure, water content and dry density distributions (Villar et al., 2005; Gen et al., 2011; Wang et al., 2013a; Saba et al., 2014a; 2014b; Bian et al., 2019; Jia et al., 2019). It was found that the blocks that were close to the technological voids swelled with a quick reduction in dry density once the technological voids were filled with water, while the dry density far from the technological voids decreased slowly (Villar et al., 2005; Gen et al., 2011; Bian et al., 2019). The swelling allowed by the technological voids significantly affected the dry density distribution and swelling capacity (Jia et al., 2019). After the filling of technological voids, the filling material with low dry density was compressed by the swelling pressure generated by the further hydration of the part with large dry density. These processes led to a relatively homogeneous distribution of dry density, and a final swelling pressure equal to that of a compacted block without technological voids, but at the same final dry density (Wang et al., 2012; Saba et al., 2014a; Bian et al., 2019). Additionally, the block fabricated by uniaxial compaction was characterized by an anisotropic microstructure that would generate a lower swelling pressure in the radial direction (Lee et al., 2012; Saba et al., 2014a). With technological

voids, the swelling anisotropy could remain to some extent after hydration and the final radial swelling pressure was mainly dominated by the final dry density, irrespective of whether there were technological voids or not (Saba et al., 2014a; Jia et al., 2019).

The aforementioned works allowed a good understanding of the effect of technological voids, but the studies were limited to the technological voids between the compacted blocks of bentonite-based materials and rigid boundaries. To the authors' knowledge, no studies have been reported on the effect of technological voids among compacted blocks, in particular the compacted blocks of bentonite and claystone mixture.

In this study, a series of infiltration tests under constant-volume condition were performed on compacted MX80 bentonite and Callovo-Oxfordian (COx) claystone mixture. The swelling pressure of compacted disks with different technological voids in between was measured in both axial and radial directions, allowing the effect of technological voids on the swelling anisotropy to be studied. Afterwards, the water content, dry density and microstructure features at different positions were investigated, helping the interpretation of the swelling behaviour of compacted mixture.

2 Materials and methods

2.1 Materials

The soil studied was a mixture of 30% (dry mass) MX80 bentonite and 70% (dry mass) crushed COx claystone mixture, which has been proposed as a candidate sealing and backfilling material by the French National Radioactive Waste Management Agency (Andra). The basic physical and chemical properties of the bentonite are summarized in Table 1. It has a montmorillonite content of 86%, a liquid limit of 494%, a plastic limit of 46% and a specific gravity of 2.76, which are in satisfactory agreement with the literature data (Tang et al., 2008; Seiphoori et al., 2014; Saba et al., 2014b). The cation exchange capacity (CEC) of the bentonite is 80 meq/100g, with Na^+ as the main exchange cation (Herbert et al., 2004; 2008; Karnland et al., 2006; Saba et al., 2014b). Fig. 1 shows the grain-size distribution determined using the conventional hydrometer method. It can be observed that the clay-size fraction (< 2 μm) is 86%.

The COx claystone was excavated from the Underground Research Laboratory (URL) in Bure and then crushed to pass through a 2 mm sieve. The main clay mineral of the COx claystone is interstratified illite-smectite (40-45%), the others being carbonates (30%), and quartz and

feldspar (25-30%) (Fouché et al., 2004). The claystone has a liquid limit of 41%, a plastic limit of 24% and a specific gravity of 2.70. The grain-size distribution determined by sedimentation reveals the clay fraction (< 2 μm) represents 26%.

The water used in this study was synthetic water (see Table 2 for the recipe of preparation), which has the same chemical composition as the pore water of COx claystone from the Andra URL in Bure. It was prepared by mixing the corresponding chemical components with de-ionized water until full dissolution (Saba et al., 2014b).

Table 1. Physical and chemical properties of MX80 bentonite

Property	Present work	Tang et al. (2008)	Seiphoori et al. (2014)	Saba et al. (2014b)	Karnland et al. (2006)	Herbert et al. (2004, 2008)
Specific gravity	2.76	2.76	2.74	2.77	-	-
Liquid limit (%)	494	520	420	575	-	-
Plastic limit (%)	46	42	65	53	-	-
Plasticity index (%)	448	478	355	522	-	-
CEC (meq/100 g)	-	-		76	80	78-85
Na^+	-	-		63	67	62.4-66.8
K^+	-	-		-	1	0.2-1.3
Mg^{2+}	-	-		-	5	3-4
Ca^{2+}	-	-		-	8	6.6-7.4
Main minerals (%)						
Montmorillonite	86	92	85		92	94
Quartz	7	3	-		3	4

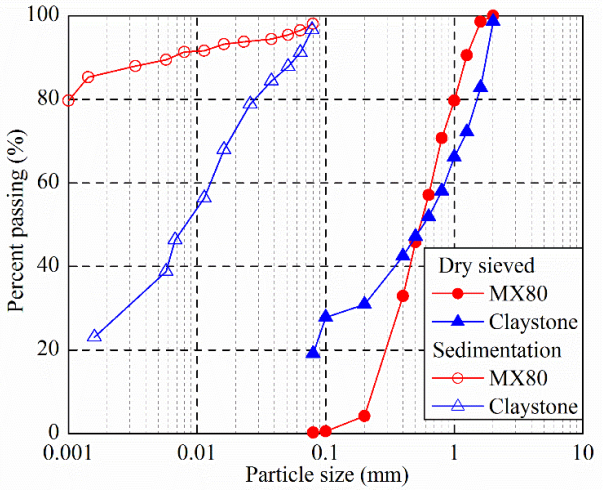

Fig. 1. Grain-size distribution of MX80 bentonite and crushed Callovo-Oxfordian (COx) claystone

Table 2. Recipe for the synthetic water preparation

Component	NaCl	$NaHCO_3$	KCl	$CaSO_4 \cdot 2H_2O$	$MgSO_4 \cdot 7H_2O$	$CaCl_2 \cdot 2H_2O$	Na_2SO_4
Content (g/L)	1.950	0.130	0.035	0.630	1.020	0.080	0.700

2.2 Test device

The layout of the experimental setup is presented in Fig. 2. The sample was placed between two porous stones in a stainless cell (50 mm in diameter). The synthetic water was injected through the bottom of the cell and the constant-volume condition was ensured by the top piston blocked with a screw. A force transducer was installed under the cell for the axial swelling pressure measurement. A total pressure sensor (6 mm in diameter) was mounted in the cell, allowing the radial swelling pressure to be monitored at one location around the perimeter of the sample. All data were recorded by a data logger. Prior to the tests, the force transducer and the pressure sensor were calibrated. The force transducer was placed on a compression machine and a series of vertical forces were applied on the measuring face of the transducer. For the pressure sensor, it was inserted in a smaller cell with a sealing plug and a series of pressures were imposed by means of a pressure-volume controller.

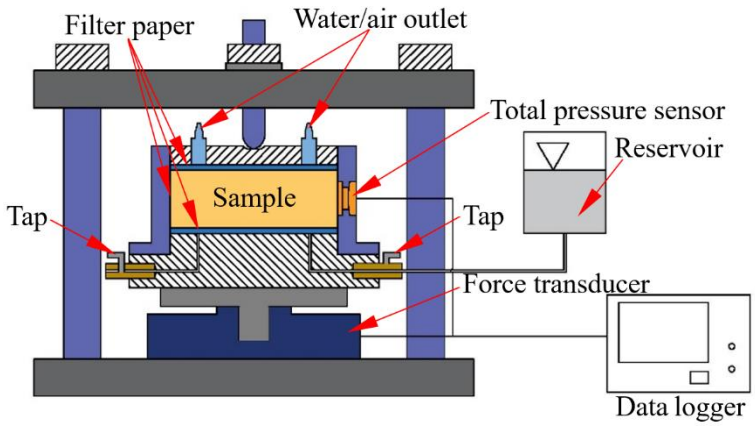

Fig. 2. Layout of the constant-volume cell for swelling pressure tests

The responses of the transducer and pressure sensor during loading-unloading paths were recorded and linear correlations between the applied force (pressure) and the output voltage were identified. Subsequently, the axial force and radial pressure were back-calculated.

2.3 Sample preparation

The bentonite and claystone powders, with initial water contents of 11.4% and 6.1%, respectively, were first mixed (30% bentonite-70% claystone in dry mass) for more than 10 min. The water content of the obtained mixture was 7.7%. Afterwards, soil disks were statically compacted using a rigid ring to reach the dimensions of 50 mm in diameter and 15 mm (for test T01) or 5 mm (for tests T02, T03, T04 and T05, see Table 3) in height, corresponding to a target dry density of 2.0 Mg/m^3.

2.4 Test procedure

For the tests with technological voids (T02, T03, T04, and T05), three identical disks with a height of 5 mm were used in each test. The lateral surfaces of all disks were first covered by filter papers. Next, the first disk was placed on a porous stone underlying a filter paper, and about 0.10 g of bentonite grains of pre-defined sizes were dispersed on the top of the first disk. Similarly, the second disk, the second bentonite grain layer, and the third disk were installed successively. Consequently, two identical layers of bentonite grains were created among three identical disks, as shown in Fig. 3a. Note that the mass of bentonite grains represented about 0.5% of all disks' mass. Thus, their contribution to the global swelling could be ignored. In this study, four groups of bentonite grains (0.25-0.40, 0.63-0.80, 1.00-1.25 and 1.60-2.00 mm) were used to create different gaps of 0.60, 0.80, 1.20 and 1.70 mm thick, corresponding to technological voids of 7.4% (T02), 9.6% (T03), 13.8% (T04) and 18.5% (T05), respectively, as summarized in Table 3. For comparison, test T01 was carried out on a compacted disk with a height of 15 mm without technological voids (Fig. 3b). Note that the total pressure sensor was located at the middle position of each sample. For the tests with technological voids, the testing surface of pressure sensor was in contact with the central disk (5 mm in thickness) and initial technological voids on the two sides of the central disk. It is believed that upon hydration, the axial swell of the compacted disks allowed the full surface of the pressure sensor to be in contact with the soils. To ensure a good contact, an initial stress of 0.05 MPa was applied.

Table 3. Test program and main results

Test	Grain size (mm)	Initial dry density of disk (Mg/m^3)	Technological voids (%)	Expected final dry density (Mg/m^3)	Final axial swelling pressure (MPa)	Final radial swelling pressure (MPa)
T01	0	2.0	0	2.0	5.22	4.46
T02	0.25-0.40	2.0	7.4	1.85	2.30	2.19
T03	0.63-0.80	2.0	9.6	1.81	1.59	1.53
T04	1.00-1.25	2.0	13.8	1.72	1.00	0.98
T05	1.60-2.00	2.0	18.5	1.63	0.53	0.53

After completion of the infiltration tests, the samples were carefully extracted from the cell. Each sample was then divided into five layers, that is, layer I to layer V, as shown in Fig. 3. For test T01, the sample was equally cut into five layers (50 mm in diameter and 3 mm in height); for tests T02, T03, T04, and T05, layers II and IV referred to the parts corresponding to technological voids and two surface layers on the two sides of the samples (1 mm thick each), other parts being termed as layer I, layer III, and layer V, respectively. Subsequently, each layer was cut into several pieces for water content and dry density measurements as well as

microstructure observation. Note that the entire operations (removal and cutting) were completed in less than 5 min to minimise water evaporation. The water content was measured by oven-drying the samples at 105 °C for 24 h and the dry density was determined based on the fluid displacement technique using a non-aromatic hydrocarbon liquid called Kerdane (Delage et al., 2008). The microstructure feature was investigated using mercury intrusion porosimetry (MIP). To minimise the microstructure disturbance during dehydration, the samples were freeze-dried (Bian et al., 2019). They were rapidly frozen using liquid nitrogen previously vacuum-cooled at its freezing point (-210 °C) and then vacuumed in a chamber for 24 h sublimation (Wang et al., 2014). For the MIP tests, the mercury intrusion pressure was limited to the range from 3.6 kPa to 228 MPa, allowing the entrance pore diameters ranging from 350 μm to 0.006 μm to be identified.

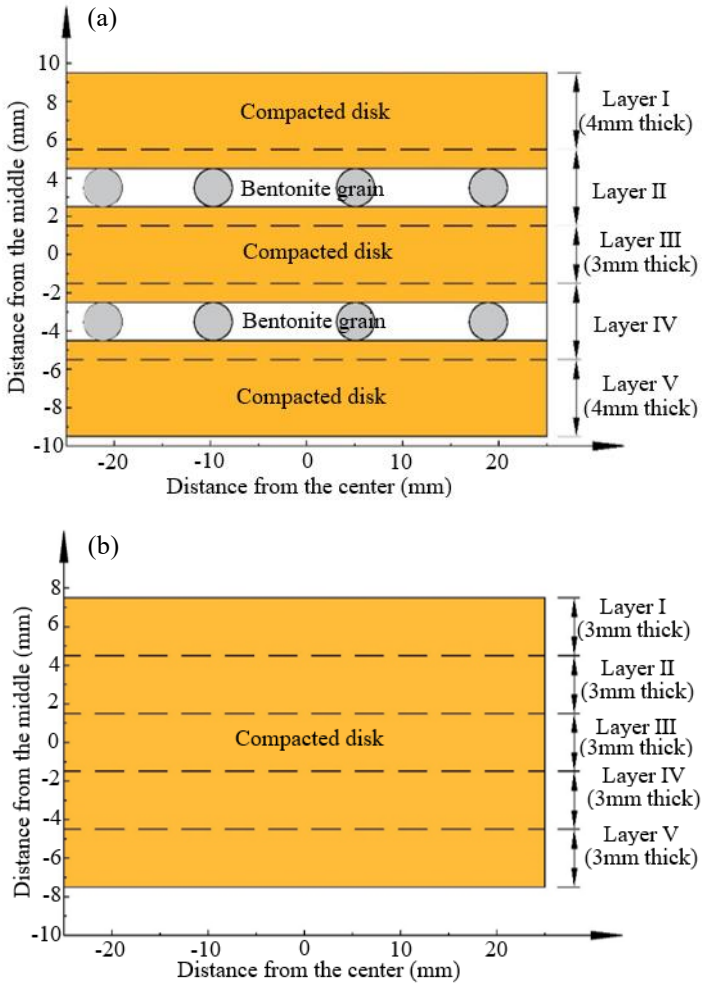

Fig. 3. Definition of sample layers: (a) T02, T03, T04, and T05, and (b) T01

3 Experimental results

3.1 Axial and radial swelling pressures

Fig. 4 depicts the evolution of axial welling pressure. For test T01, the axial swelling pressure started with a fast increase and then reached stabilization at 5.22 MPa (Fig. 4c). For tests T02, T03, T04, and T05 with technological voids, the axial pressures decreased slightly from the initial value (0.05 MPa) to about 0.047 MPa at the beginning of hydration (0.09, 0.11, 0.20, and 0.48 h for tests T02, T03, T04, and T05, respectively) (Fig. 4a). This phenomenon could be attributed to the softening of bentonite grains during hydration. After that, the axial swelling pressures tended to increase at an increasing rate till the inflection points at 5.2, 6.2, 6.6, and 7.0 h for T02, T03, T04, and T05, respectively (Fig. 4a and b). The variation rates then decreased to zero after 49.0, 45.4, 37.5, and 35.3 h, with the axial swelling pressures reaching stabilization at 2.30, 1.59, 1.00, and 0.53 MPa for tests T02, T03, T04, and T05, respectively (Fig. 4b and c). On the whole, the larger the technological voids, the lower the variation rate and the lower the final axial swelling pressure.

The evolution of radial swelling pressure is shown in Fig. 5. A first quick increase was observed at the beginning for all tests, at almost the same rate (Fig. 5a). For test T01, the radial swelling pressure increased rapidly and then reached a stabilization value of 4.46 MPa (Fig. 5b and c). For tests T02, T03, T04 and T05, the radial swelling pressures, after the first quick increases, reached the peak values of 3.02, 2.55, 2.01, and 1.74 MPa, respectively, after about 2 h, then decreased significantly until about 6.5 h hydration (Fig. 5a and b). Afterwards, they increased again, but slowly and reached stabilization at 2.19, 1.53, 0.98, and 0.53 MPa after 48.7, 45.3, 38.2, and 34.4 h, respectively (Fig. 5b and c). The times needed to decrease from the peaks to the minimum values coincided with the inflection points identified on the axial swelling pressure curves (Figs. 4a and 5a). Moreover, the times required to attain the stabilization of axial and radial swelling pressures are almost the same. The final values of axial and radial swelling pressures are summarized in Table 3 and the variations of the axial and radial swelling pressures with technological voids are presented in Fig. 6. It can be observed that both axial and radial swelling pressures decreased with increasing technological voids, indicating that the presence of technological voids reduced the swelling capacity of the mixture.

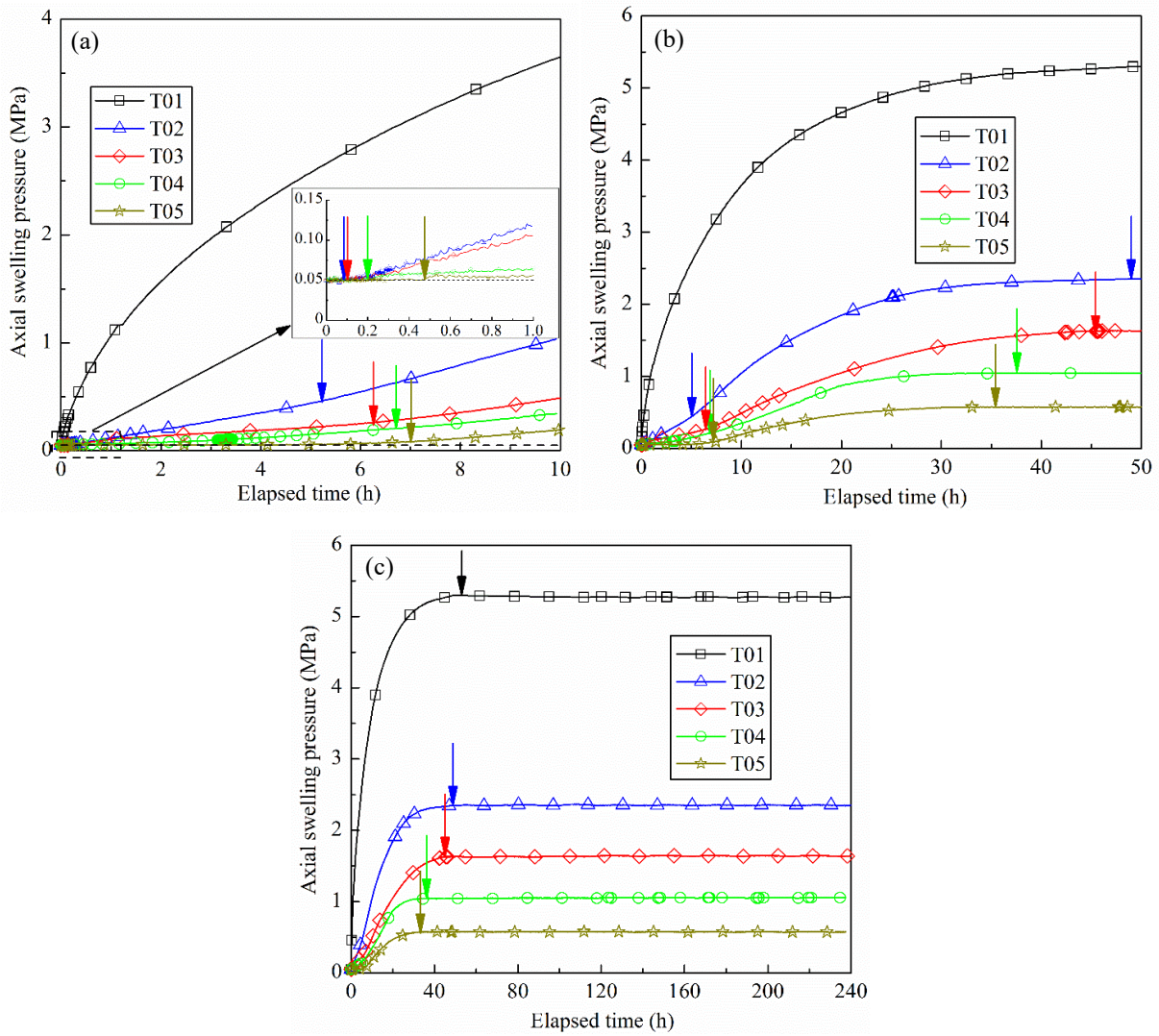

Fig. 4. Evolution of axial swelling pressure (a) in the first 10 h, (b) in the first 50 h, and (c) for the whole test duration. Note: the curves in the figure are drawn according to all the measurement points but only a few symbols in each curve are plotted for distinction purpose

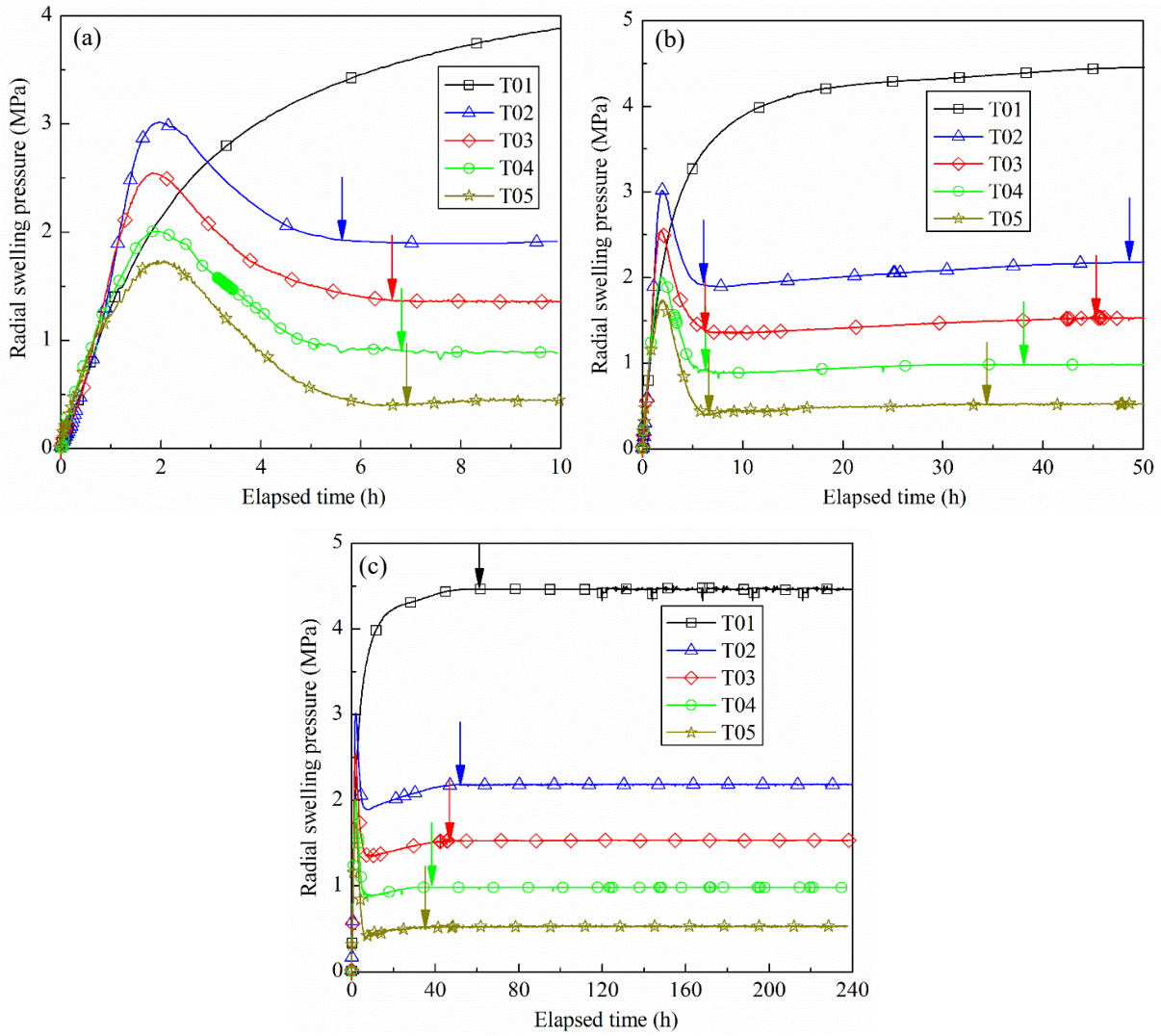

Fig. 5. Evolution of radial swelling pressure (a) in the first 10 h, (b) in the first 50 h, and (c) for the whole test duration

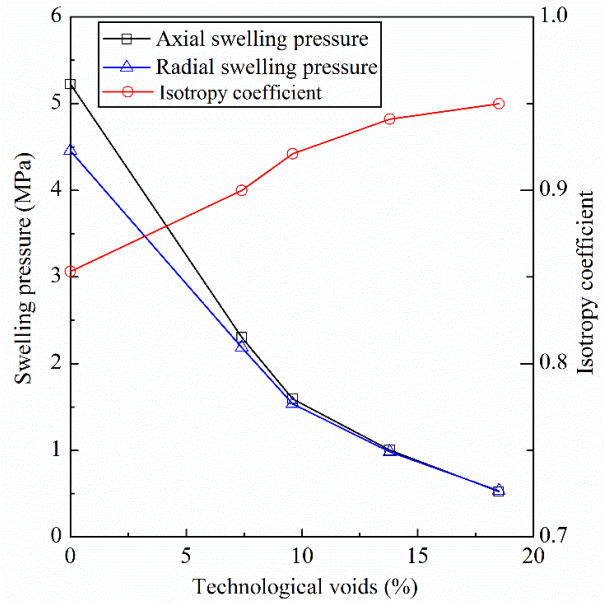

Fig. 6. Relationship between final swelling pressures, isotropy coefficient and technological voids

3.2 Water content and dry density profiles

The water content and dry density profiles are plotted in Fig. 7. Both water content and dry density profiles were almost symmetrical with respect to the horizontal plans in the middle of the samples. For sample T01, the water content and dry density were characterized by the increase and decrease trends with the increasing distance from the symmetry plan. For samples T02, T03, T04, and T05, the filling of technological voids led to heterogeneous distributions of water content and dry density, with larger water contents and lower dry densities for layers II and IV that included technological voids, but lower water contents and larger dry densities for layers I, III and V. Further examination showed that the dry density of layer III was larger than those of layers I and V. This could be attributed to the longer wetting path and slower swelling of layer III when the technological voids were closed. On the whole, the larger the technological voids, the more heterogeneous the distributions of water content and dry density. The expected final dry densities calculated using the total volume including technological voids are also presented in Fig. 7b. It appears that for sample T01 without technological voids, the measured values were quite close to the expected final value, while for other samples with technological voids the measured values are little different from the expected final one, revealing the effect of technological voids.

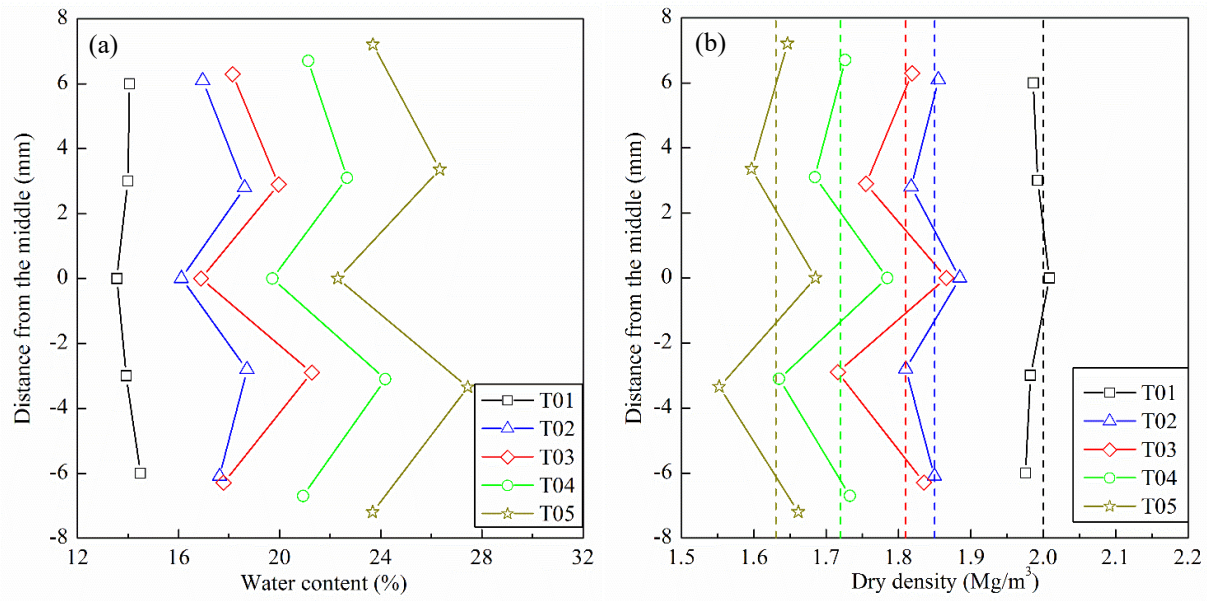

Fig. 7. Water content and dry density profiles after tests: (a) water content profile and (b) dry density profile

3.3 Microstructure distribution

Fig. 8 shows the results from MIP tests on samples T01, T02, T03, T04, and T05. The result of the as-compacted sample is also presented for comparison. For sample T01, the cumulative

curves of all layers were almost the same; on the contrary, samples T02, T03, T04, and T05 exhibited significantly different microstructures: the cumulative curves of layers II and IV with technological voids lied above those of other layers, which was consistent with the dry density distributions. Note that the final intruded void ratio was slightly smaller than the corresponding ones determined on the large layer specimens. This was attributed to the inaccessible pores which could not be identified with the maximum pressure applied in the MIP tests (Tang et al., 2011; Wang et al., 2014).

From the pore size density function curves (Fig. 8b), it was observed that the as-compacted sample presented a typical bimodal porosity with a mean size of 0.02 μm for the small-pore population and a mean pore size of 5 μm for the large-pore population, respectively. After water saturation, the mean size of large-pore population increased sharply from 5 to 15-30 μm, while the mean size of small-pore population kept almost constant. For the samples with technological voids, a new pore population with a mean size of 0.1-0.3 μm appeared, leading to tri-modal pore size distribution curves (Fig. 8d, f, h and j).

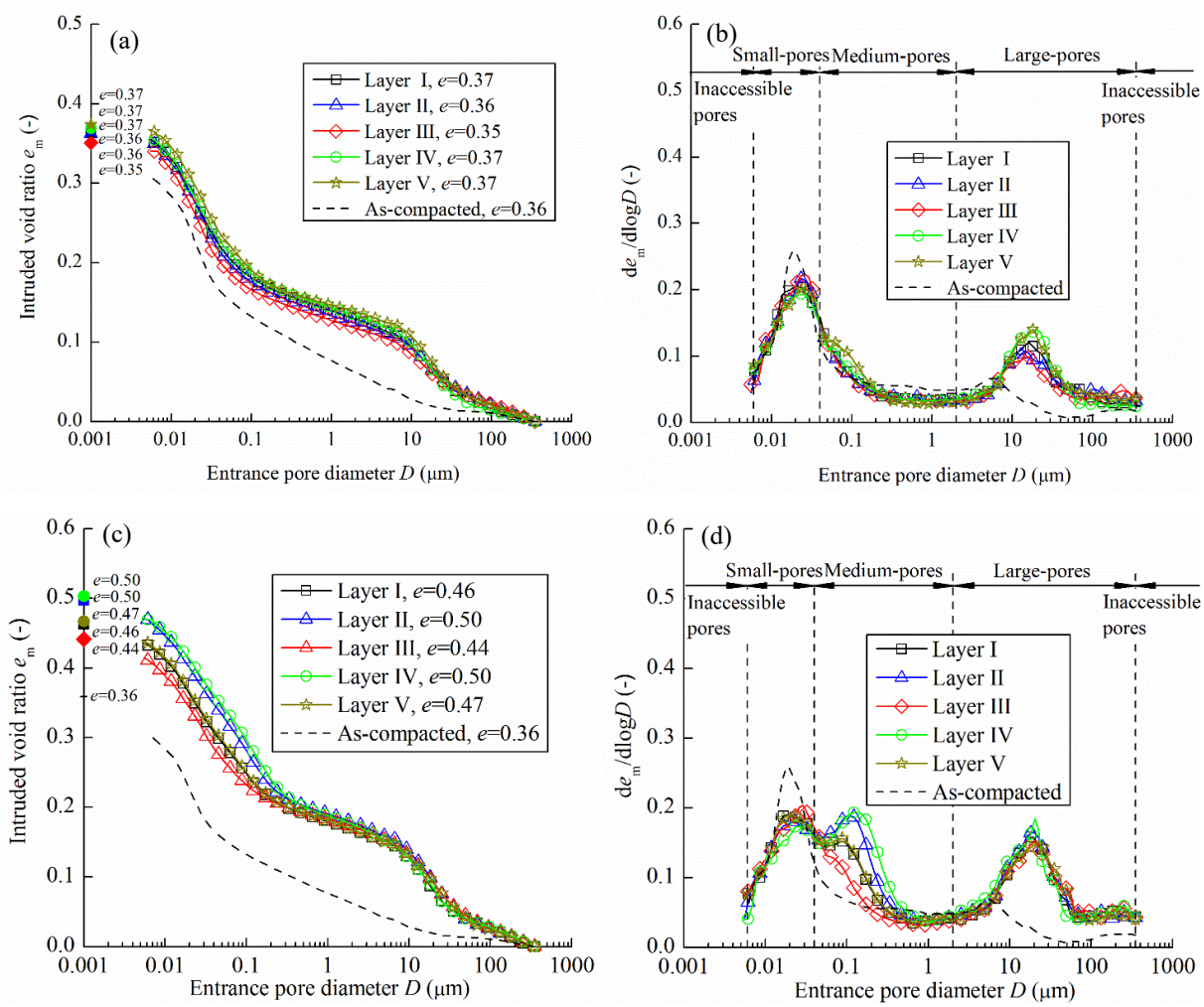

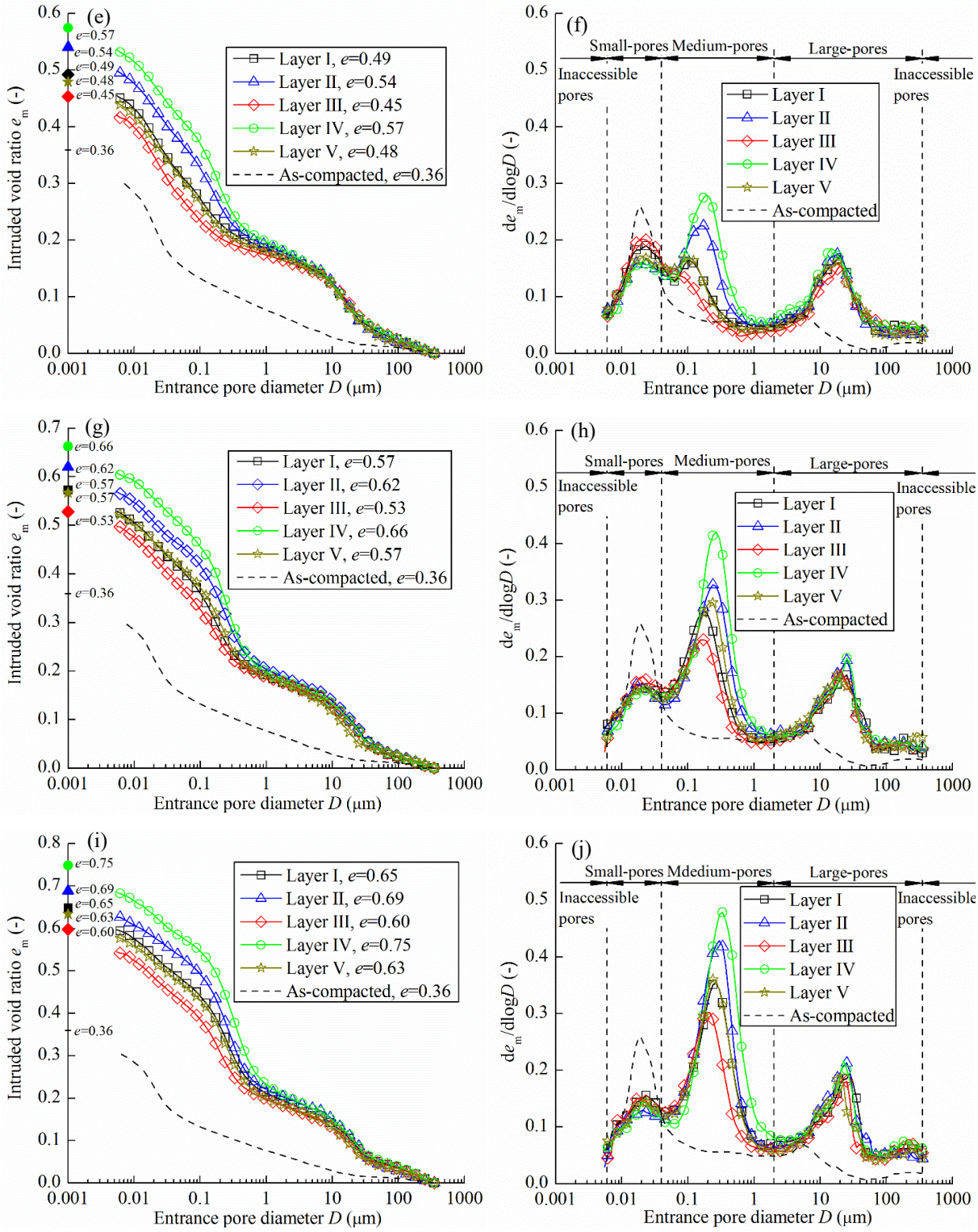

Fig. 8. Pore size distribution at different layers: (a) cumulative curves of T01, (b) density function curves of T01, (c) cumulative curves of T02, (d) density function curves of T02, (e) cumulative curves of T03, (f) density function curves of T03, (g) cumulative curves of T04, (h) density function curves of T04, (i) cumulative curves of T05, and (j) density function curves of T05

To further analyze the different microstructure features, four pore types were defined: inaccessible pores (< 0.006 μm and > 350 μm), small pores (0.006-0.04 μm), medium pores

(0.04-2 μm) and large pores (2-350 μm), as shown in Fig. 8 (Wang et al., 2014; Bian et al., 2019). Fig. 9 presents the variations of void ratios corresponding to different pores with the distance from the middle of samples. It shows clearly that the void ratios for the four types of pores were almost the same for sample T01 without technological voids. By contrast, for the samples with technological voids (T02, T03, T04, and T05), larger inaccessible-pore, medium-pore and large-pore void ratios and a lower small-pore void ratio were observed for layers II and IV, which were characterized by higher water contents and lower dry densities.

Fig. 10 compares the pore size distribution curves from different tests for different layers. The corresponding changes in the void ratio of different pore types are also presented in Fig. 11. It can be seen that the technological voids increased the sizes of large-pores and medium-pores, without significantly modifying the size of small-pores. As the technological voids increased, the large-pore, medium-pore and inaccessible-pore void ratios increased, while the small-pore void ratio decreased slightly. Further examination showed that the variation of the medium-pore void ratio was the most pronounced, suggesting that the heterogeneous microstructure distribution due to the presence of technological voids was mainly related to changes in medium pores.

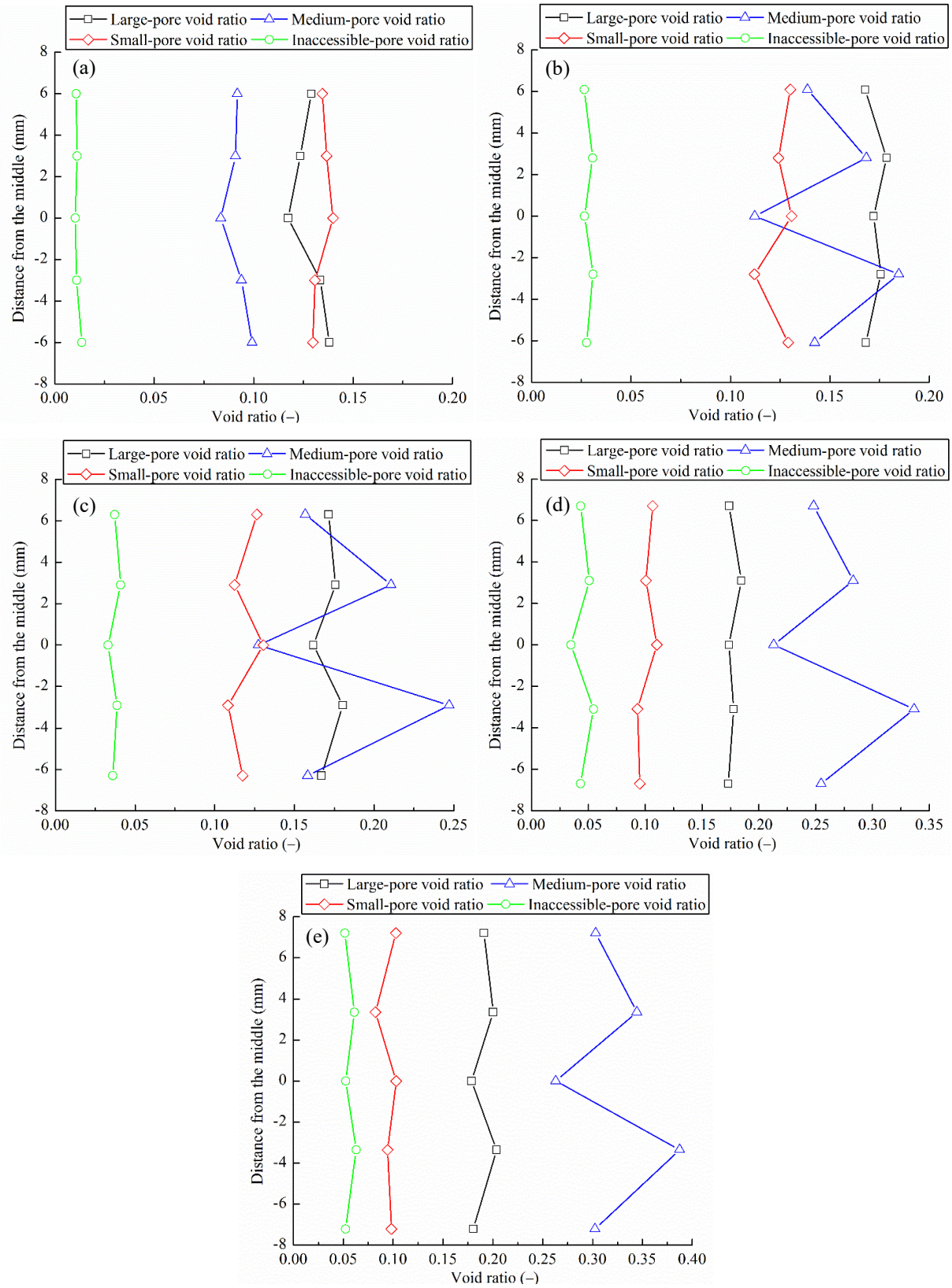

Fig. 9. Changes in inaccessible-pore, small-pore, medium-pore and large-pore void ratios (a) T01, (b) T02, (c) T03, (d) T04 and (e) T05

4 Interpretation and discussion

The evolution of axial and radial swelling pressures is basically linked to the microstructural changes (Saba et al., 2014a). According to the swelling pressures kinetics, the hydration of the samples with technological voids (T02, T03, T04, and T05) could be divided into four stages, namely stages I, II, III, and IV, respectively, as shown in Fig. 12 for sample T04 as an example. At stage I, the bentonite grains were softened, resulting in a slight decrease of axial pressure and at the same time, the disks swelled and started to fill the technological voids. At stage II, the adjacent disks came in contact with each other with more significant development of axial swelling pressure. During stages I and II, radial swelling pressure increased quickly and then decreased significantly, exhibiting a marked peak. This could be explained as follows: due to the presence of technological voids, the central disk, which was in contact with the radial pressure sensor, swelled significantly in the axial direction and reduced the soil dry density in the vicinity of radial sensor, resulting in a decrease of the radial swelling pressure. When the decrease in radial pressure due to the axial swelling was larger than the increase due to radial swelling, a peak on the radial swelling pressure curve appeared. When the technological voids were fully filled and sealed with further hydration, the soils were subjected to swelling under constant-volume condition, and the radial swelling pressure increased again at stage III and tended to be stable at stage IV. By contrast, the axial swelling pressure increased at a much higher rate at stage III and then reached stabilization at stage IV. During stages III and IV, the samples became more and more homogenous. Summarizing, stages I and II referred to a filling process of technological voids, while stages III and IV could be regarded as a homogenization process. During the homogenization process, the sample could be divided into two zones: (i) a swelling zone at which the soil with a dry density larger than the expected final one underwent further swelling and thus further decrease of dry density; (ii) a sealing zone where the soil with a dry density lower than the expected final one was subjected to compression imposed by the further swelling of soil in the swelling zone (Bian et al., 2019). From Fig. 7b, it appears that layers I, III, and V corresponded to the swelling zone, while the sealing zone included layers II and IV where the technological voids were preset. For the sample with larger technological voids, a much longer time was required to reach the full homogenization owing to the lower swelling pressure of the sample, which could be evidenced by the lower increase rate of the axial swelling pressure (Fig. 4b and c).

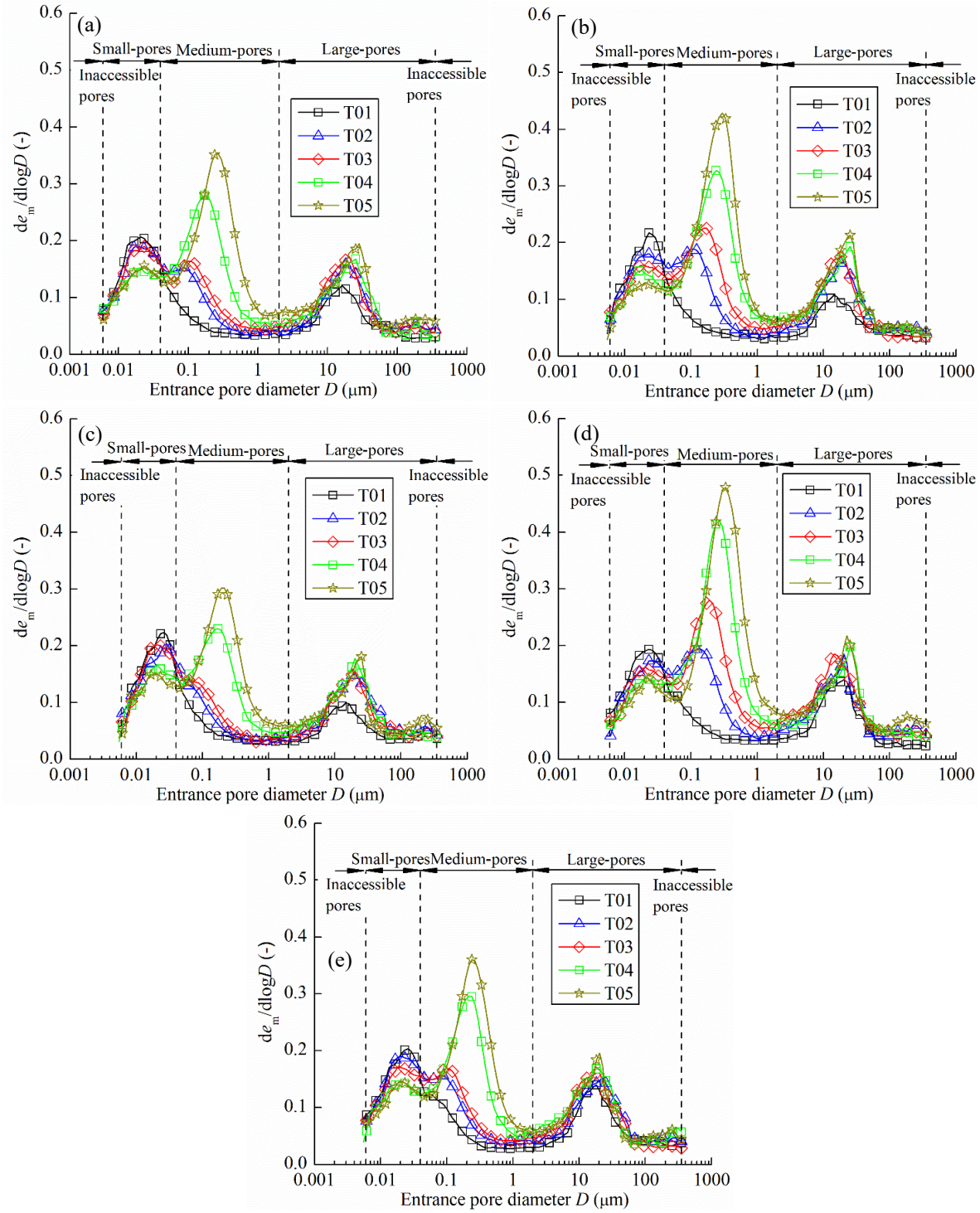

Fig. 10. Pore size distributions for (a) layer I, (b) layer II, (c) layer III, (d) layer IV, and (e) layer V

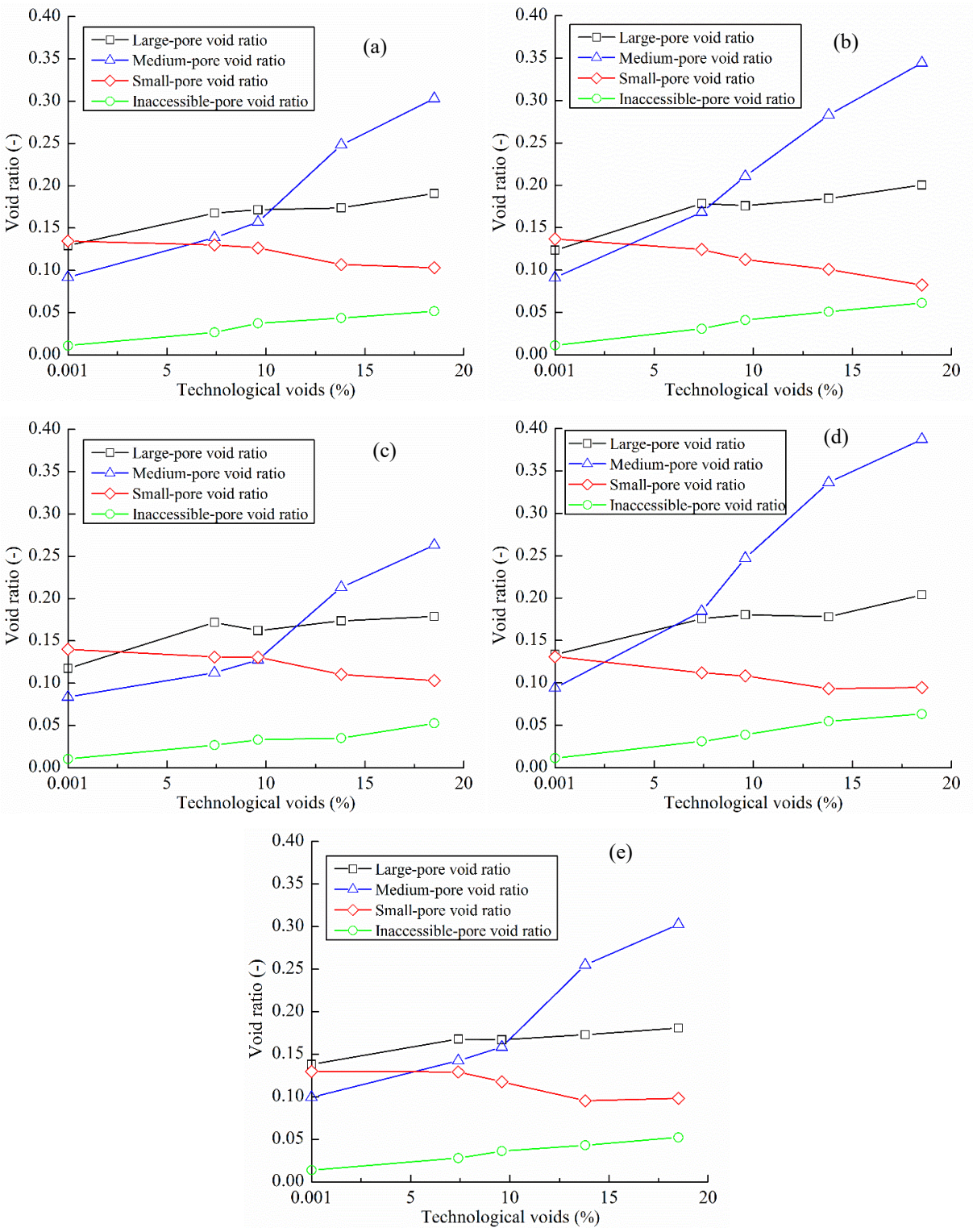

Fig. 11. Changes in inaccessible-pore, small-pore, medium-pore and large-pore void ratios with technological voids for (a) layer I, (b) layer II, (c) layer III, (d) layer IV and (e) layer V

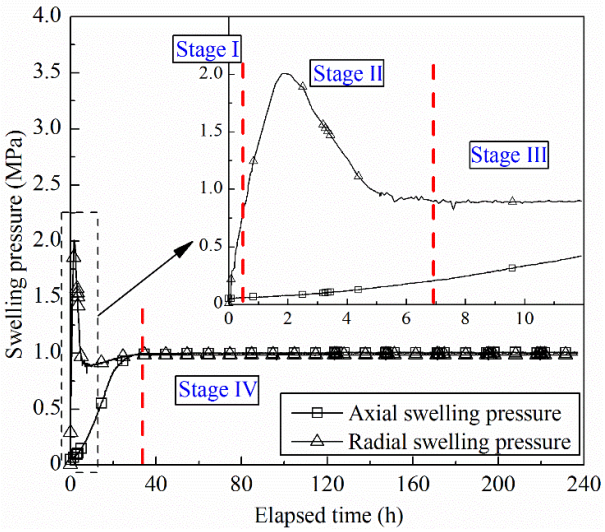

Fig. 12. Schematic diagram showing separation of the four swelling stages

From Figs. 7 and 9, it appears that the variations of small-pore void ratios along the samples exhibited a trend similar to that of dry density while those of inaccessible-pore, medium-pore and large-pore void ratios exhibited an opposite one, indicating a good correspondence between the microstructure and dry density. Fig. 13 displays the variations of the void ratios of inaccessible, small, medium and large pores with dry density. It clearly shows that the inaccessible-pore, medium-pore and large-pore volume increased with the decreasing dry density, while the small-pore volume decreased. Upon hydration, water molecules were adsorbed by clay particles, layer after layer up to four layers, resulting in an increase in interparticle space. This pore size change corresponded to the inaccessible pores and could not be detected by MIP (Wang et al., 2014). Obviously, this process highly depended on the soil dry density. The soils with low dry density allowed more water infiltration into the interlayer space, and therefore exhibited more inaccessible pores. Meanwhile, the enlargement of inter-particle space upon saturation could facilitate the exfoliation of clay particles and lead to large-pore filling. Additionally, fissure-like 2-dimensional (2-D) pores would appear owing to the division of soil aggregates, resulting in an increase of large-pore volume (Wang et al., 2014). The lower the dry density, the larger the 2-D pores, explaining the increase of the mean size of large pores with the increasing technological voids (Fig. 10). The increase of large-pore void ratio was the combined effect of the two aforementioned mechanisms. In addition to the absorption of water molecules in the interlayer space, the subdivision of particles into thinner ones could enlarge the interparticle pores inside the aggregates, resulting in a decrease of small-pore void ratio (Delage 2007). Regarding the creation of new pore population (medium pores), it was aided by the filling of large pores and enlargement of small pores.

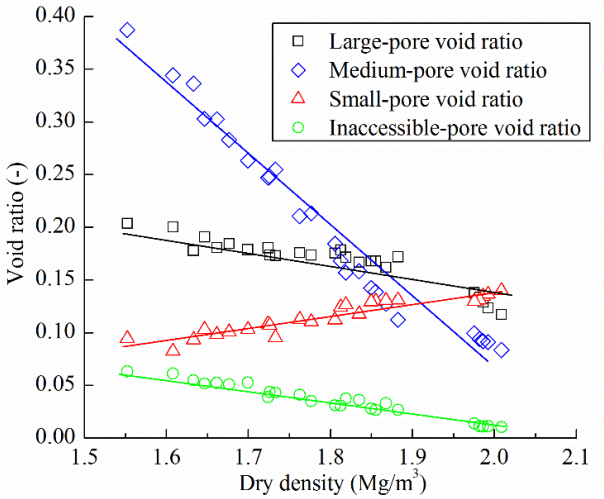

Fig. 13. Large-pore, medium-pore, small-pore and inaccessible-pore void ratios versus soil dry density

For the samples with technological voids, larger inaccessible-pore, medium-pore and large-pore void ratios and a lower small-pore void ratio were observed in the sealing zone (layers II and IV). As the hydration time increased, the medium pores and large pores in the sealing zone were compressed by swelling pressure, leading to decreases in medium-pore and large-pore void ratios. By contrast, in the swelling zone, the inaccessible-pore void ratio increased while the small-pore void ratio decreased due to more water driven into the interparticle pores with time (Wang et al., 2014). Consequently, these processes resulted in a more uniform microstructure.

As remarked earlier, the axial swelling pressures reached stabilization after 49.0, 45.4, 37.5, and 35.3 h hydration for tests T02, T03, T03, and T05, respectively, although the distributions of dry density and microstructure still changed with time. To address this remark, the measured axial swelling pressure is plotted versus the expected final dry density for all tests in Fig. 14. For comparison, the variation of axial swelling pressure with the dry density of the same material (30/70 MX80 bentonite-COx claystone mixture) without technological voids is also presented (Zeng et al., 2019). All data remarkably agreed, providing a unique relationship between the axial swelling pressure ($P_{\text{s-axial}}$) and the final dry density (ρ_{d}):

$$P_{\text{s-axial}}=1.564\times10^{-5}\exp^{6.390\rho_{\text{d}}} \quad (1)$$

This agreement confirmed that the axial swelling pressure at stabilization is not affected by the heterogeneity of the samples induced by technological voids. In other words, the technological voids played the same role as the macropores of the compacted samples without technological voids. As far as the difference of swelling pressures in the axial and radial directions was concerned, it could be observed that the radial swelling pressure (4.46 MPa) was significantly smaller than the axial swelling pressure (5.22 MPa) for the sample without technological voids

(Fig. 6). To further analyse this anisotropic behaviour, an isotropy coefficient was defined as the ratio of radial to axial swelling pressures. Because, for the samples with technological voids, the dry density distribution was still heterogeneous along the sample height at the end of infiltration tests (Fig. 7b), the measured value of radial swelling pressure could be dependent on the measurement position. Based on the division of the samples for dry density measurement (Fig. 3a), the testing surface of pressure sensor was in contact with the soils at layers II, III, and IV and the dry density of soils in the vicinity of the pressure sensor $\rho_{\text{d-sensor}}$ could be calculated using Eq. (2):

$$\rho_{\text{d-sensor}}=(\rho_{\text{d-III}}\times A_3+\rho_{\text{d-II}}\times A_2+\rho_{\text{d-IV}}\times A_4)/(A_2+A_3+A_4) \quad (2)$$

where $\rho_{\text{d-II}}$, $\rho_{\text{d-III}}$, and $\rho_{\text{d-IV}}$ are the dry densities of layers II, III, and IV; A_2, A_3, and A_4 are the areas of contact between the pressure sensor and layers II, III, and IV, respectively. In this study, A_2, A_3, and A_4 are equal to 17.22, 5.23, and 5.23 mm^2, respectively. According to the dry density distribution of soils, the values of dry density of soils in contact with the radial sensor were estimated to be 1.87, 1.81, 1.74, and 1.64 Mg/m^3 for tests T02, T03, T04, and T05, respectively. Correspondingly, the axial swelling pressures of the soils in contact with the pressure sensor were estimated to be 2.43, 1.67, 1.05, and 0.56 MPa from Eq. (1). The isotropy coefficients for the samples with technological voids were determined according to the axial and radial swelling pressures of the soils in contact with the pressure sensor. The relationship between the isotropy coefficient and technological voids is presented in Fig. 6. It appears that the samples with technological voids exhibited higher isotropy coefficients, compared to that without technological voids (0.85). Moreover, the larger the technological voids, the larger the isotropy coefficient. As explained by Lee et al. (2012), Saba et al. (2014a) and Jia et al. (2018), the anisotropic behaviour of compacted disks could be attributed to the microstructural anisotropy induced by the uniaxial compaction. After compaction, clay particles were preferentially oriented in the horizontal direction. Upon hydration, the samples exhibited more significant swelling in the axial direction. For the samples with technological voids, aggregates swelled and split up upon hydration, filling the technological voids and allowing the rearrangement of clay particles. This process led to a microstructural collapse and reduced the initial orientation of aggregates due to the uniaxial compaction (Saba, 2013).

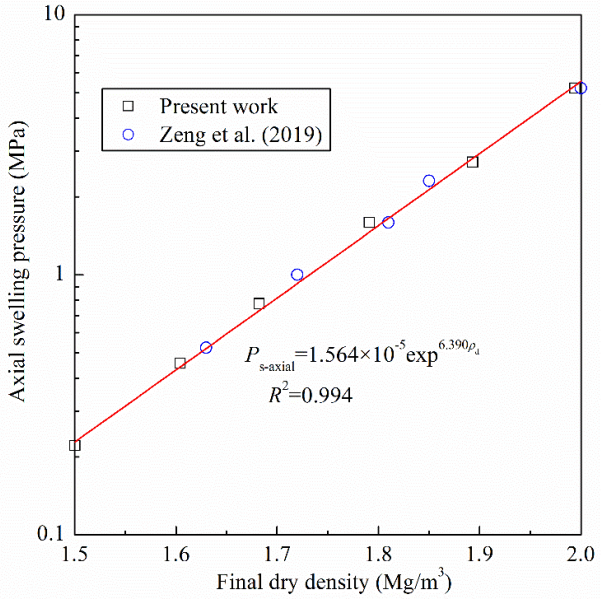

Fig. 14. Relationship between axial swelling pressure and final dry density

From a practical point of view, swelling pressure and hydraulic conductivity are two key parameters in the design of sealing and backfilling materials and in the assessment of their long-term sealing performance. Given that the presence of technological void can reduce the initial anisotropy and result in a relatively isotropic swelling, the corresponding axial and radial swelling pressure can be satisfactorily predicted according to the unique relationship elaborated between the axial swelling pressure and the expected final dry density when the initial state of compacted disks and the technological voids are known.

In general, water transfer is primarily dominated by the network of large pores (> 2 μm) (Wang et al., 2013b). As mentioned above, the large-pore void ratio is greater in the sealing zone corresponding to the technological voids and a larger hydraulic conductivity can be expected in this zone. Therefore, possible preferential flow in the radial direction can appear in the sealing zone and should be taken into account, at least in the short term. In the long term, these large pores can be compressed by swelling pressure, resulting in a decrease of hydraulic conductivity in the sealing zone.

5 Conclusions

The effect of technological voids on the swelling behaviour of compacted MX80 bentonite-COx claystone was investigated by carrying out infiltration tests under constant-volume condition and microstructure observation. From the experimental results, the following conclusions can be drawn.

Two main processes were identified from the kinetics of axial and radial swelling pressures of the samples with technological voids: (i) a filling process of technological voids and (ii) a homogenization process. During the homogenization process, there were sealing and swelling zones. The former referred to the initial technological voids zone, while the latter to the zone far from the initial technological voids zone.

At the end of tests, water content and dry density distributions were still heterogeneous, with a larger water content and a lower dry density in the sealing zone while a lower water content and higher dry density in the swelling zone. The sealing zone was characterized by larger inaccessible-pore (< 0.006 μm and > 350 μm), medium-pore (0.04-2 μm) and large-pore (2-350 μm) void ratios and a lower small-pore (0.006-0.04 μm) void ratio. It was believed that the difference in dry density and microstructure between the sealing and swelling zones decreased with the hydration time, rendering the sample more and more homogeneous.

The final axial and radial swelling pressures decreased with increasing technological voids. The relationship between the axial swelling pressures and the expected final dry density could be described by a unique correlation, which was in good agreement with that for compacted disks. The isotropy coefficient (ratio of radial to axial swelling pressures) increased with the increasing technological voids from 0 to 18.5%.

Acknowledgments

The authors thank the China Scholarship Council (CSC). The supports provided by Ecole des Ponts ParisTech and the French National Radioactive Waste Management Agency (Andra) are also greatly acknowledged.

References

Bian, X., Cui, Y.J., and Li, X.Z. 2019. Voids effect on the swelling behaviour of compacted bentonite. Géotechnique, 69(7): 593-605.

Cui, Y.J. 2017. On the hydro-mechanical behavior of MX80 bentonite-based materials. Journal of Rock Mechanics and Geotechnical Engineering, 9(3): 565-574.

Delage, P. 2007. Microstructure features in the behaviour of engineered barriers for nuclear waste disposal. Experimental unsaturated soil mechanics, 11-32.

Delage, P., Le, T.T., Tang, A.M., Cui, Y.J., and Li, X.L. 2008. Suction effects in deep Boom clay block samples. Géotechnique 57(2): 239–244.

Dixon, D.A., Gray, M.N., and Thomas, A.W. 1985. A study of the compaction properties of potential clay-sand buffer mixtures for use in nuclear fuel waste disposal. Eng. Geol. 21(3/4): 247-255.

Fouché, O., Wright, H., Le Cléac'h, J.M., and Pellenard, P. 2004. Fabric control on strain and rupture of heterogeneous shale samples by using a non-conventional mechanical test. Applied Clay Science, 26(1-4): 367-387.

Gens, A., Vállejan, B., Sánchez, M., Imbert, C., Villar, M. V., and Van Geetl, M. 2011. Hydromechanical behaviour of a heterogeneous compacted soil: experimental observations and modelling. Géotechnique 61(5): 367-386.

Herbert, H.J., Kasbohm, J., Moog, H.C., and Henning, K.H. 2004. Long-term behaviour of the Wyoming bentonite MX-80 in high saline solutions. Applied Clay Science, 26(1-4): 275-291.

Herbert, H.J., Kasbohm, J., Sprenger, H., Fernández, A.M., and Reichelt, C. 2008. Swelling pressures of MX-80 bentonite in solutions of different ionic strength. Physics and Chemistry of the Earth, Parts A/B/C, 33: S327-S342.

Jia, L.Y., Chen, Y.G., Ye, W.M., and Cui, Y.J. 2019. Effects of a simulated gap on anisotropic swelling pressure of compacted GMZ bentonite. Engineering geology, 248: 155-163.

Karnland, O., Olsson, S., and Nilsson, U. 2006. Mineralogy and sealing properties of various bentonites and smectite-rich clay materials. Technical Report No. TR-06-30. SKB, Swedish Nuclear Fuel and Waste Management Co.

Komine, H., and Ogata, N. 1994. Experimental study on swelling characteristics of compacted bentonite. Canadian Geotechnical Journal, 31(4): 478-490.

Komine, H., and Ogata, N. 1999. Experimental study on swelling characteristics of sand-bentonite mixture for nuclear waste disposal. Soils and Foundations, 39(2): 83-97.

Lee, J.O., Lim, J.G., Kang, I.M., and Kwon, S. 2012. Swelling pressures of compacted Ca-bentonite. Engineering Geology, 129: 20-26.

Pusch, R. 1982. Mineral–water interactions and their influence on the physical behavior of highly compacted Na bentonite. Canadian Geotechnical Journal, 19(3): 381-387.

Saba, S. 2013. Hydro-mechanical behaviour of bentonite-sand mixture used as sealing materials in radioactive waste disposal galleries (Doctoral dissertation, Université Paris-Est).

Saba, S., Barnichon, J. D., Cui, Y. J., Tang, A. M., and Delage, P. 2014a. Microstructure and anisotropic swelling behaviour of compacted bentonite/sand mixture. Journal of Rock Mechanics and Geotechnical Engineering, 6(2): 126-132.

Saba, S., Cui, Y.J., Tang, A.M., and Barnichon, J.D. 2014b. Investigation of the swelling behaviour of compacted bentonite–sand mixture by mock-up tests. Canadian Geotechnical Journal, 51(12): 1399-1412.

Seiphoori, A., Ferrari, A., and Laloui, L. 2014. Water retention behaviour and microstructural

evolution of MX-80 bentonite during wetting and drying cycles. Géotechnique, 64(9): 721-734.

Tang, A.M., Cui, Y.J., Le, T.T., 2008. A study on the thermal conductivity of compacted bentonites. Applied Clay Science, 41 (3-4): 181–189.

Tang, C.S., Tang, A.M., Cui, Y.J., Delage, P., Schroeder, C., and Shi, B. 2011. A study of the hydro-mechanical behaviour of compacted crushed argillite. Engineering Geology, 118(3-4): 93-103.

Villar, M.V., García-Siñeriz, J.L., Bárcena, I., and Lloret, A. 2005. State of the bentonite barrier after five years operation of an in situ test simulating a high level radioactive waste repository. Engineering Geology, 80(3-4): 175-198.

Wang, Q., Tang, A.M., Cui, Y.J., Delage, P., and Gatmiri, B. 2012. Experimental study on the swelling behaviour of bentonite/claystone mixture. Engineering Geology, 124: 59-66.

Wang, Q., Tang, A.M., Cui, Y.J., Delage, P., Barnichon, J.D. and Ye, W.M. 2013a. The effects of technological voids on the hydro-mechanical behaviour of compacted bentonite–sand mixture. Soils and Foundations, 53(2): 232-245.

Wang, Q., Cui, Y.J., Tang, A.M., Barnichon, J.D., Saba, S., and Ye, W.M. 2013b. Hydraulic conductivity and microstructure changes of compacted bentonite/sand mixture during hydration. Engineering Geology: 164, 67-76.

Wang, Q., Cui, Y.J., Tang, A.M., Li, X.L., and Ye, W.M. 2014. Time-and density-dependent microstructure features of compacted bentonite. Soils and Foundations, 54(4): 657-666.

Zeng, Z.X., Cui, Y.J., Zhang, F., Conil, N., and Talandier, J. 2019. Investigation of swelling pressure of bentonite/claystone mixture in the full range of bentonite fraction. Applied Clay Science. doi: 10.1016/j.clay.2019.105137.